International Journal of Heat and Mass Transfer 145 (2019) 118738

Contents lists available at ScienceDirect

International Journal of Heat and Mass Transfer

journal homepage: www.elsevier.com/locate/ijhmt

Addressing the adverse cold air inflow effects for a short natural draft dry cooling tower through swirl generation

Yuchen Dai [a,*], Antonio S. Kaiser [b], Yuanshen Lu [a], Alexander Y. Klimenko [a], Peixin Dong [a], Kamel Hooman [a]

[a] School of Mechanical and Mining Engineering, The University of Queensland, Brisbane, Australia
[b] Department of Thermal and Fluids Engineering, Universidad Politécnica de Cartagena, Doctor Fleming s/n, 30202 Cartagena, Spain

ARTICLE INFO

Article history:
Received 15 July 2019
Received in revised form 10 September 2019
Accepted 12 September 2019
Available online 30 September 2019

Keywords:
Cold inflow
Boundary layer separation
Buoyancy
Cooling tower
Swirl

ABSTRACT

Short natural draft dry cooling towers (NDDCTs) are susceptible to cold air inflow. A transient simulation on Gatton tower is carried out to study the time-dependent cold air inflow characteristic. Our results show that, the cold air inflow penetrates inside the tower after a short period of pseudo-steady state, and a steady state with the cold air inflow is finally formed. We also investigate the possibility of inducing swirling motions to counter the cold inflow. The results demonstrate that, by reducing the local vortices caused by the specific tower structure, and thinning the boundary layer thickness, swirl is able to decrease the cold air inflow effect. Finally, feasibility of the suggested approach was verified by comparing the energy required to create the swirl with the extra heat transfer from the heat exchangers in the tower which would have not been materialized because of the cold inflow. It was observed that, an extra 40 kW heat transfer gain can be anticipated if only 1 W is spent to induce the swirl.

1. Introduction

Australia has 1.2-GW of off-grid diesel generation, in the sub-10 MWe range, serving mining sites and remote communities [1]. This unique topology encourages research and development of small scale power generation systems. Replacing such small power plants, compared to the existing coal-fired plants which generate multiples of 100 MWe, with renewable counterparts is a current research and development challenge. This is mainly because all the components, including the cooling towers, have to scale down. Under this circumstance, a 20-m-height NDDCT has been designed and built in the Gatton campus at the University of Queensland. Our experimental measurements have illustrated certain differences between short natural draft cooling towers [2] and the tall (over 100 m) counterparts [3], including the influence of crosswind [4,5], and the cold air inflow under windless conditions [6,7]. For cooling towers with the airflow relatively slow, the flow will separate from the tower wall before the plume leaves the tower; hence the penetration of the cold ambient air into the tower. This phenomenon has been observed in our full-scale tower experiments conducted under windless conditions, and led to a non-negligible deteriorating effect on the performance of the cooling tower [6].

Cold inflow not only occurs in cooling towers, but in all of the buoyant flows in open-topped vessels once the updraft velocity is weak. The penetration depth of the cold inflow was first experimentally determined by Jörg and Scorer [8]. Those authors conducted tests on downward jets of saline water into a fresh water tank to observe that, the cold inflow penetration depends on the Reynolds number, the Froude number, duct height-to-diameter ratio, upstream velocity profile, wall roughness and heat transfer through the duct wall. Specifically, the empirical formula proposed by them of the cold inflow penetration depth for cases with turbulent boundary layers on a smooth wall can be expressed as:

$$\frac{g\beta\Delta T\nu}{\left[\left(\frac{H_p}{D}\right)^2+8\right]^3 u_z^3}=10^{-6} \tag{1}$$

This formula can be also expressed as:

$$\frac{H_p}{H}=\frac{D}{H}\left[10^2\left(\frac{g\beta\Delta TD}{u_z^2}\right)^{\frac{1}{3}}\left(\frac{\nu}{u_zD}\right)^{\frac{1}{3}}-8\right]^{\frac{1}{2}}=\frac{1}{Ar}\left[10^2(FrRe)^{-\frac{1}{3}}-8\right]^{\frac{1}{2}} \tag{2}$$

which indicates that the dimensionless cold air inflow penetration depth is inversely proportional to the aspect ratio, Froude number and Reynolds number, and a critical axial velocity, at which cold air inflow just occurs, can be found by putting $H_p = 0$. However, as those authors mentioned, a reduction on the boundary layer thickness results in a decrease on the critical axial velocity.

* Corresponding author.
E-mail address: yuchen.dai@uq.edu.au (Y. Dai).

https://doi.org/10.1016/j.ijheatmasstransfer.2019.118738
0017-9310/

Nomenclature

Acronyms

Ar	aspect ratio
c_p	specific heat capacity, $J/(kg \cdot K)$
D	diameter, m
Fr	Froude number
Fs	Safety factor
g	acceleration of gravity, m/s^2
H	height, m
k	turbulence kinetic energy, m^2/s^2
m	mass flow rate, kg/s
N	Order of accuracy
P	pressure, Pa
Pr	Prandtl number
Q	heat transfer rate, kW
r	radius, m
Rc	Convergence ratio
Re	Reynolds number
Rf	Refinement factor
Ro	Rossby number
t	time, s
T	temperature, K
u	velocity, m/s
V	volume, m^3
W	width, m
z	elevation, m

Greek letters

α	thermal diffusivity, m^2/s
β	thermal expansion coefficient, 1/K
ϵ	dissipation rate, m^2/s^3
ν	kinematic viscosity, m^2/s
ω	vorticity, 1/s
Φ	dimensionless source intensity
ϕ	source term, N/m^3
ρ	density, kg/m^3

Subscripts

0	ambient
bl	bottom layer
e	effective
hx	heat exchanger
ml	middle layer
p	penetration
r, θ, z	radial, tangential, axial direction
t	turbulent
tl	top layer
to	tower outlet
tw	tower

Modi and Moore [9] theoretically examined the cold inflow penetration depth on a laminar boundary layer of a buoyant flow in a vertical channel. Based on their assumptions and limits on the Reynolds number and the Froude number, the dimensionless penetration depth was found to vary as $Fr^{16/9}/Re^{1/9}$. The lab-scale experiments indicated that the cold inflow is time-dependent, and it arises from the boundary layer separation in the near-exit region [10]. The numerical results demonstrated that, at low Reynolds number, the penetration depth of the cold inflow varies as a function of the Rayleigh number consistent with the previous experimental observation by Sparrow et al. [11]. A laminar flow was also modelled in a solar chimney, examining that the cold inflow penetration depth mainly depends on the Rayleigh number in the limit of low Reynolds numbers [12]. The cold inflow impact on the performance of a chimney was also reported by Fisher and Torrance [13]. In their study, the heat transfer was decreased by the cold inflow by approximately 4%. This might be explained by the low Rayleigh number in natural convection pertinent to their small-scale experiment. Chu and Rahman [14] studied the cold inflow impact in an NDDCT with a low Froude number. The lab-scale experiments results indicated that the cold inflow decreases the mass flow rate through the tower by at least 45%. This is significant as the heat transfer from a tower is linearly proportional to the mass flow rate. Hence, it makes perfect engineering sense to minimize the cold inflow.

One approach addressing the cold air inflow effect is to narrow the tower exit diameter and thus increase the dynamic pressure [15]. Alternatively, the flow field can be modified by inserting objects along the flow channel. Chu et al. [16,17] proposed a method by installing a wire mesh screen on the top of the cooling tower to reduce the cold inflow. The lab-scale experiments showed that cold inflow was significantly prevented using wire mesh with an appropriate size, which balances the draft loss caused by the extra resistance and the cold inflow prevention by the boundary layer thickness reduction.

Since the cold air inflow phenomenon always accompanies with boundary layer separations, controlling flow separations should be investigated as means to reduce the cold inflow effect. It was both experimentally and numerically proven that flow separations in conical diffusers with certain angles can be reduced by introducing swirling motions at the inlet of diffusers as the resultant centrifugal force thins the boundary layer to the wall [18,19]. However, with strong swirl intensities, a reversed flow at the centreline will be inevitable, leading to a recirculation zone at the outlet of the diffuser [20]. As a result of the presence of the reversed flow, the mass flow rate through the diffuser will be decreased. Hence, it is necessary to prevent the occurrence of the reversed flow caused by intensive swirl for the performance of the device. Clausen et al. [21] measured a swirl boundary layer developing in a conical diffuser. Those authors found a range of swirl intensity which is of sufficient magnitude to avert boundary layer separation but insufficient to cause reversed flow in the core region. Senoo et al. [22] experimentally found suitable swirl intensities that not only eliminate boundary layer separations but avoid the recirculation at the centreline. Armfield et al. [23,24] employed k-ϵ and an algebraic Reynolds stress turbulence models to predict moderate swirl interacting with boundary layer separations. Their results showed that the modified k-ϵ model and algebraic Reynolds stress turbulence model give better predictions than the standard k-ϵ model. They also indicated the two-layer model, rather than sing-layer model or wall functions, is found to be necessary to accurately predict the level, location, and the axial variation of the near-wall peak in turbulence quantities for swirling flows. Kurkin and Shakhov [25] further compared the algebraic and modified k-ϵ turbulence model on a swirling diffuser, at which the rotational motion is created by rotating the wall. Their verification show that the modified k-ϵ turbulence model is slightly better than the algebraic one. In addition to numerical and experimental studies on turbulent swirling flows interacting with boundary layer separations, theoretical methods were however found to be inappropriate due to the limitation on inviscid assumptions [26].

Swirl is also able to reduce the boundary layer thickness, as theoretically demonstrated by Najafi et al. [27], and thinning boundary layer thickness also has a favourable effect on reducing the cold air inflow as indicated in [12,16]. Maddahian et al. [28] compared two typical swirl, namely, the forced vortex and free vortex swirl, by conducting an analytical solution. Their results indicated that, the decrease in boundary layer thickness highly depends on the local swirl intensity in the edge of the boundary layer, and thus the forced vortex swirl provides more decreases in the boundary layer thickness. A large swirl intensity, not large enough to create the reversed flow at the centreline, also stimulates more updraft motions by changing the vorticity field as demonstrated by Klimenko [29]. Thus, it is worthy introducing swirl inside the tower and investigating how it interacts with the cold air inflow.

Swirl has been applied in a natural draft wet cooling tower (NDDWT) to increase the homogeneity of the flow and to reduce the crosswind throttling effect [30,31]. Our previous study has also introduced swirl in an NDDCT to enhance the mass flow rate and thus improve the performance of the tower [32]. However, no reference has been provided illustrating how swirl interacts with the cold inflow in short cooling towers. Hence, this paper will fill this gap in the literature.

2. Physical model

2.1. Facility description and physical domain

The computational object is a 20 m height NDDCT in hyperbolic shape as shown in Fig. 1. The detailed parameters can be found in [6].

2.2. Governing equations

The incompressible flow is assumed since the airflow speed inside and outside the tower is far lower than 0.3 Mach number. The Boussinesq's approximation is introduced in the vertical component of the momentum equations to reflect the buoyancy effect caused by the density difference. In this study, all the cases are investigated on the no wind condition. In addition, the computational domain, tower structure, heat exchanger, solid ring, as well as source zone are all geometrically axisymmetric. Hence, the axisymmetric assumption is made and the model is simulated by solving a series of conservation equations of physical quantities as:

Incompressible continuity equation:

$$\frac{\partial(ru_r)}{\partial r}+\frac{\partial(ru_z)}{\partial z}=0 \tag{3}$$

Radial component of momentum conservation:

$$\frac{\partial u_r}{\partial t}+\frac{1}{r}\frac{\partial}{\partial r}(ru_ru_r)+\frac{\partial}{\partial z}(u_ru_z)=-\frac{1}{\rho}\frac{\partial P}{\partial r}+\frac{u_\theta^2}{r}+\frac{1}{r}\frac{\partial}{\partial r}\left(2r\nu_e\frac{\partial u_r}{\partial r}\right)-2\nu_e\frac{u_r}{r^2}+\frac{\partial}{\partial z}\left[\nu_e\left(\frac{\partial u_r}{\partial z}+\frac{\partial u_z}{\partial r}\right)\right] \tag{4}$$

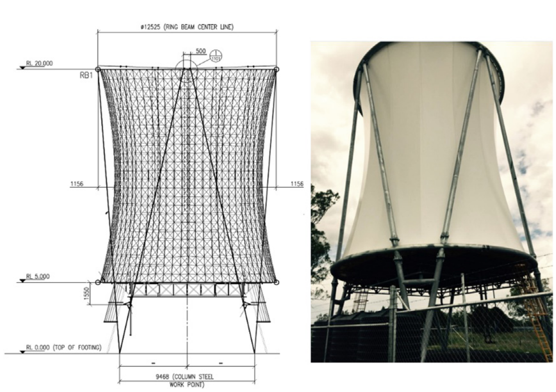

Fig. 1. Physical model and domain of the NDDCT.

Tangential component of momentum conservation:

$$\frac{\partial u_\theta}{\partial t}+\frac{1}{r}\frac{\partial}{\partial r}(ru_ru_\theta)+\frac{\partial}{\partial z}(u_\theta u_z)=-\frac{u_ru_\theta}{r}+\frac{1}{r^2}\frac{\partial}{\partial r}\left[r^3\nu_e\frac{\partial}{\partial r}\left(\frac{u_\theta}{r}\right)\right]+\frac{\partial}{\partial z}\left(\nu_e\frac{\partial u_\theta}{\partial z}\right) \tag{5}$$

Axial component of momentum conservation:

$$\frac{\partial u_z}{\partial t}+\frac{1}{r}\frac{\partial}{\partial r}(ru_ru_z)+\frac{\partial}{\partial z}(u_zu_z)=g\beta(T-T_0)+\frac{1}{r}\frac{\partial}{\partial r}\left[r\nu_e\left(\frac{\partial u_r}{\partial z}+\frac{\partial u_z}{\partial r}\right)\right]+\frac{\partial}{\partial z}\left(2\nu_e\frac{\partial u_z}{\partial z}\right) \tag{6}$$

Energy conservation:

$$\frac{\partial T}{\partial t}+u_r\frac{\partial T}{\partial r}+u_z\frac{\partial T}{\partial z}=\frac{1}{r}\frac{\partial}{\partial r}\left[\left(\alpha+\frac{\nu_t}{Pr_t}\right)r\frac{\partial T}{\partial r}\right]+\frac{\partial}{\partial z}\left[\left(\alpha+\frac{\nu_t}{Pr_t}\right)\frac{\partial T}{\partial z}\right] \tag{7}$$

where

$$\nu_e=\nu+\nu_t \tag{8}$$

The k-ϵ realizable turbulence model is employed in this work since it has been proved to perform better predictions than the standard one for flows involving swirl, boundary layers under strong adverse pressure gradients, separations, and recirculation, as indicated in [33]. The realizable version relates the turbulent kinematic viscosity to the turbulent kinetic energy k and the dissipation rate ϵ via:

$$\nu_t=C_\mu\frac{k^2}{\epsilon} \tag{9}$$

and determines the distribution of k and ϵ from the following transport equations.

$$\frac{\partial k}{\partial t}+\frac{\partial u_zk}{\partial z}+\frac{1}{r}\frac{\partial ru_rk}{\partial r}=\frac{\partial}{\partial z}\left[\left(\nu+\frac{\nu_t}{\sigma_k}\right)\frac{\partial k}{\partial z}\right]+\frac{1}{r}\frac{\partial}{\partial r}\left[\left(\nu+\frac{\nu_t}{\sigma_k}\right)r\frac{\partial k}{\partial r}\right]+\frac{G_k}{\rho}+\frac{G_b}{\rho}-\epsilon-\frac{Y_M}{\rho}+\frac{S_k}{\rho} \tag{10}$$

$$\frac{\partial \epsilon}{\partial t}+\frac{\partial u_z\epsilon}{\partial z}+\frac{1}{r}\frac{\partial ru_r\epsilon}{\partial r}=\frac{\partial}{\partial z}\left[\left(\nu+\frac{\nu_t}{\sigma_\epsilon}\right)\frac{\partial \epsilon}{\partial z}\right]+\frac{1}{r}\frac{\partial}{\partial r}\left[\left(\nu+\frac{\nu_t}{\sigma_\epsilon}\right)r\frac{\partial \epsilon}{\partial r}\right]+C_1S_\epsilon-C_2\frac{\epsilon^2}{k+\sqrt{\nu\epsilon}}+C_{1\epsilon}\frac{\epsilon}{k}C_{3\epsilon}\frac{G_b}{\rho}+\frac{S_\epsilon}{\rho} \tag{11}$$

where $C_{1\epsilon}=1.44, C_2=1.68, \sigma_k=1.0, \sigma_\epsilon=1.2$. More details about the model could be referred in FLUENT Guide [34].

The swirl is introduced by adding source term ϕ_θ as an external force at the tangential component of the momentum equations. The conventional swirl ratio, like Rossby number or Swirl number, is not adopted in this work because neither the axial nor the swirl velocity profile can be known in advance. Instead, we employed another dimensionless number with input parameters to represent the swirl intensity as:

$$\Phi_\theta=\frac{\phi_\theta}{\rho g\beta(T_{hx}-T_0)} \tag{12}$$

which relates to the Rossby number Ro as

$$Ro=\frac{u_z}{r\omega_z}\sim\frac{1}{\Phi_\theta^{\frac{1}{2}}} \tag{13}$$

since

$$\phi_\theta\sim\frac{\rho u_\theta^2}{r}\sim\rho r\omega_z^2 \tag{14}$$

As the flow is developing inside the tower, the tangential velocity is also influenced by the initial condition, mixing losses, as well as the swirl decay along the tower wall [35].

3. Numerical model

Fig. 2 is presented to show the computational domain which is extended well beyond and above the actual tower. A 2-D axisymmetric numerical method is applied here similar to [36,37]. As illustrated by Fig. 2(a), a solid ring is applied around the heat exchanger to simulate a solid obstruction in the same location of the real tower. Industrial heat exchanger bundles rectangular in shape (so is the projected area for a V-frame or A-frame bundle) while the tower base is circular. For a horizontal arrangement of the bundles, parts of the tower circular cross-sectional area remain uncovered. It is therefore a common practice to use solid obstructions to cover this section in order to avoid mixing of the heated air above the cooling tower with the cold air upstream. The width of the solid ring is determined by the effective frontal area of the real tower [6]. The swirl is then generated by adding tangential momentum in a source zone right above the solid ring with height H_ϕ, while its width W_ϕ remains the same as the solid ring. Hence, the aspect ratio of the source zone is introduced as:

$$Ar_\phi = \frac{H_\phi}{W_\phi} \tag{15}$$

The computational domain, corresponding to the optimal geometry as well as size indicated in our previous study [6], is illustrated in Fig. 2(b). We are studying the case at the no wind condition. As a result, the pressure inlet, instead of velocity inlet, is chosen to be the inlet boundary condition, since only the pressure is known as the atmospheric pressure far away from the cooling tower. In addition, it is reasonable to estimate a very low turbulence level due to the free stream at the inlet flow and thus the turbulence intensity as well as the turbulence viscosity ratio are prescribed to be 1% and 1, respectively, referring to ANSYS FLUENT Guide [34]. The porous media zone method is adopted to model the heat exchangers based on the pressure loss coefficient, and associated with the radiator boundary condition on its upper surface [38].

ANSYS FLUENT 18.0 is employed to simulate the transient fluid flow process. It has been indicated that the standard k-ϵ model is capable and suitable of achieving the requirement of numerical studies on NDDCTs [39,40]. However, neither cold air inflows nor swirling motions were investigated in their work. Thus, a modified turbulence model is required to capture those additional characteristics in this study. In comparison with the standard k-ϵ model, the k-ϵ realizable model provides improved prediction for flows involving swirl, boundary layers under strong adverse pressure gradients, separations, and recirculation, as indicated in [33]. In addition to the the k-ϵ realizable model, the RNG k-ϵ model as well as Reynolds stress model have also been proved to perform better in swirling flows than the standard k-ϵ model. It should be noted our previous experiment data on the cooling tower do not contain any swirling motions. Hence, only numerical predictions on the cold inflow phenomenon based on the k-ϵ realizable model, RNG k-ϵ model, and Reynolds stress model are compared. The temperature contour associated with vectors are collected at steady state with the input parameters, including the heat rejection rate and ambient temperature, prescribed in accordance with the

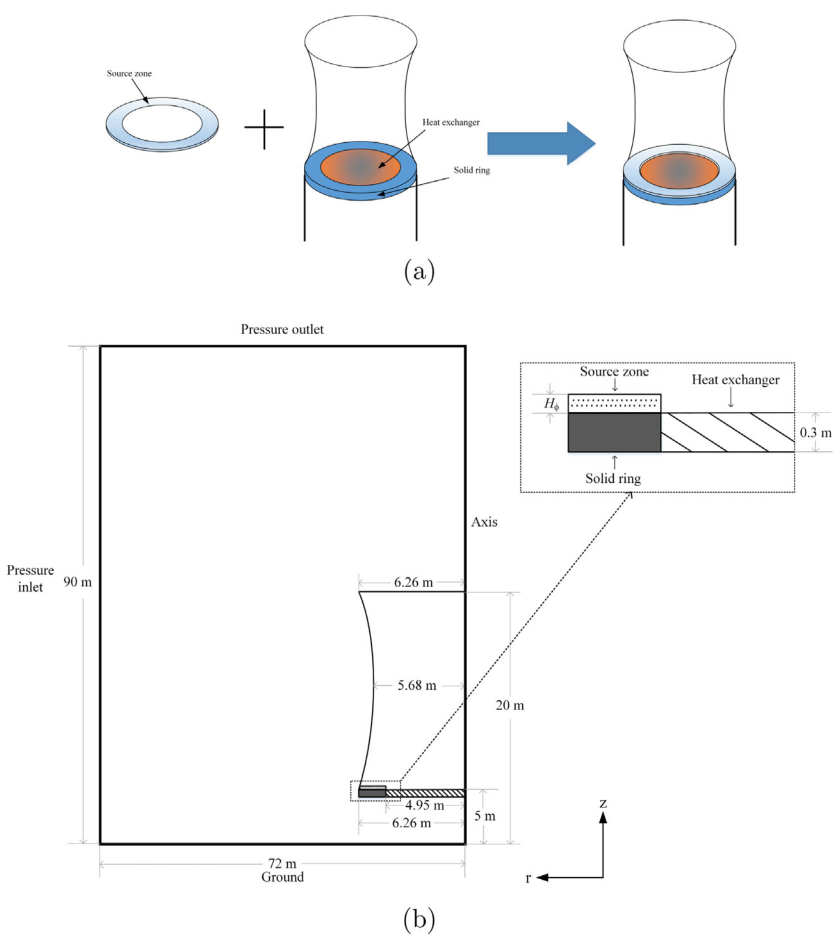

Fig. 2. Schematic of the NDDCT: (a) numerical model; (b) computational domain.

experiment data when cold inflow occurs [6]. As seen in Fig. 3, both the k-ϵ realizable model and RNG k-ϵ model are able to capture the cold air inflow phenomenon while the Reynolds stress model cannot. A further comparison of the k-ϵ realizable model and RNG k-ϵ model with the experiment data are conducted in the next section, concluding the k-ϵ realizable model, instead of the RNG k-ϵ model, is the suitable choice in our cases. Besides, the k-ϵ realizable model owes the best convergence performance among these models. Hence, it is finally selected in this work.

A comparison study among the discretization schemes for convection terms is carried out. As indicated by [41,42], the difference between the second-order scheme and higher order schemes for convection terms is negligible for low swirl intensities while it becomes large when swirl intensity increases and quite significant with highly swirling flows. Since the swirl intensity in this study cannot be quantified like the conventional swirling inlet flows, a comparison among the schemes is necessary. Fig. 4 shows the comparison among the schemes including the first-order upwind, second-order upwind, QUICK, and third-order MUSCL. The tangential velocity profile, in the case with the largest swirl intensity ($\Phi_0 = 4$) adopted in this study, at the tower outlet is selected for the comparison. The radius is normalized by the total radius of the tower outlet, while the tangential velocity is normalized by the buoyancy term. As seen, the first-order upwind scheme represents a major difference from others, while the difference among the second-order upwind, QUICK, and third-order MUSCL schemes is quite small. Thus, the second-order upwind scheme is selected for convection terms in this study.

The enhanced wall treatment (EWT) has been adopted in this numerical study. When the near-wall mesh is fine enough to resolve the viscous layer (the first near-wall node placed at $y^+ \approx 1$, which has been applied in this work though it imposes too large a computational requirement), the EWT is identical to the conventional two-layer zonal model, which combines the k-ϵ realizable model at the fully turbulent region with a one-equation model at the near-wall region. Studies on the comparison among the two-layer model, low-Reynolds-number models and wall functions when dealing with the turbulence at the near-wall region have been conducted by Chen et al. [43] and Rodi [44]. Cases including strong pressure gradient, surface curvatures, boundary layers, and separations, etc. were selected. Their conclusions indicated that, both two-layer model and low-Reynolds-number model show better performance than wall functions, while the two-layer model outperforms the low-Reynolds-number model from both numerical and physical viewpoints [43]. Specifically, when dealing with boundary layers with highly adverse pressure gradients, i.e. boundary layer separations, the two-layer model has relative merits in comparison with low-Reynolds-number models or wall functions [44]. Since the cold air inflow arises from boundary layer separation, the enhanced wall treatment with $y^+ \approx 1$, resulting in the two-layer model, is selected in the numerical work.

The air thermo-physical properties are taken to be constant except for the density, as modelled by the Boussinesq approximation. The ambient temperature and heat exchanger temperature are 20 °C and 60 °C, respectively. As a preliminary study, the off-design conditions, including crosswind and outdoor temperature effects, are not included, but further investigations will be conducted in the later work. The heat transfer coefficient and resistance of the heat exchanger are based on experimental data in [6].

The total heat transfer can be given by:

$$Q_{hx} = m_{air} c_p (T_{air} - T_0) \tag{16}$$

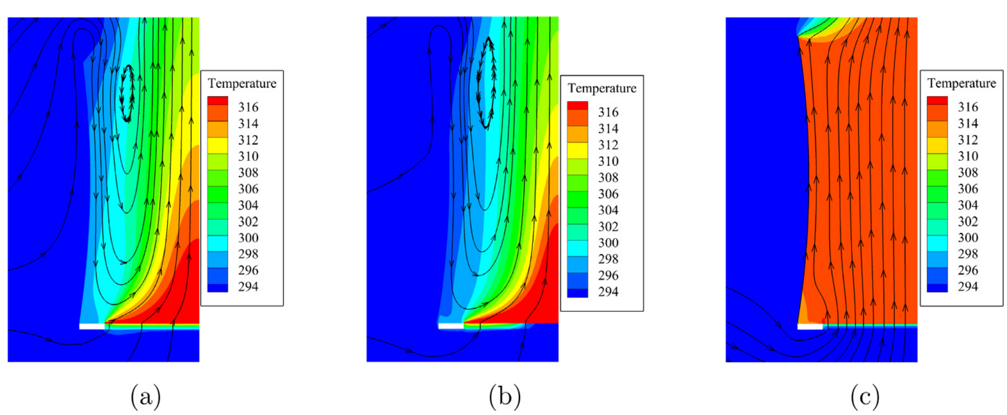

Fig. 3. Temperature contour associated with vectors at steady state: (a) k-ϵ realizable model; (b) RNG k-ϵ model; (c) Reynolds stress model.

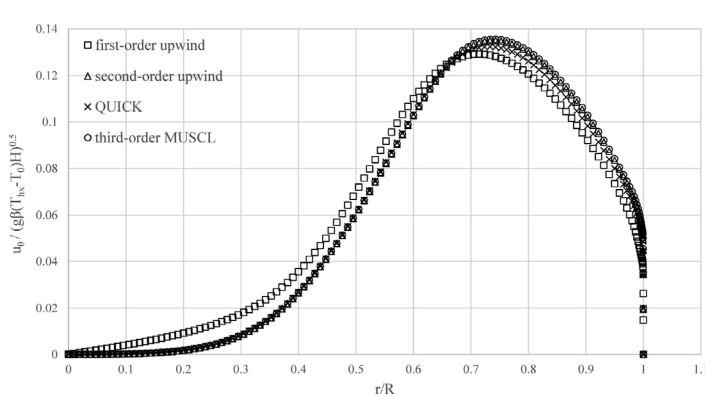

Fig. 4. Comparison on the swirl velocity profile among cases with discretization schemes for the convection terms.

The time step is specified by the Courant-Friedrichs-Lewy condition as:

$$\Delta t = \frac{CFL\Delta z_{min}}{u_{z,avg}} \tag{17}$$

where CFL is Courant-Friedrichs-Lewy number and it equals 5 in this study in accordance with [45]. Besides, according to our previous study [6], the average axial velocity through the heat exchanger at no wind conditions is about 0.7 m/s. Combining with the minimum size of the grid on axial direction Δz_{min}, the time step is finally determined as 0.05 s.

The Grid Convergence Index (GCI) [46] is employed for the grid independency analysis. Four sets of grid (coarse to fine) are selected with refinement factors higher than 1.3. Three key area-averaged mean variables collected at the tower outlet, including the axial velocity, swirl velocity, and temperature, for each GCI test are compared. It should be mentioned that, in the GCI test, the data are collected at steady state with the prescribed swirl intensity ($\Phi_\theta = 4$). The GCI can be expressed as:

$$GCI_{i+1,i} = \frac{Fs}{Rf^N - 1}\left|\frac{f_{i+1} - f_i}{f_i}\right| \tag{18}$$

where f is the key variable; Fs is the safety factor and it has been recommended to be 1.25 when three or more meshes are available [46]; Rf is the refinement factor; N is the order of accuracy and it is expressed as:

$$N = ln\left(\frac{1}{Rc_i}\right) \Big/ ln(Rf) \tag{19}$$

where Rc_i is the convergence ratio and is written for the i^{th} mesh as:

$$Rc_i = \frac{f_i - f_{i-1}}{f_{i+1} - f_i} \tag{20}$$

It should be noted all the calculated convergence ratio values are between 0 and 1, so that monotonic convergences are guaranteed. The results are listed in Table 1. As seen, all the GCI values decrease with the refinement of the mesh. The major differences are among the axial velocity GCI. The third mesh with 48,375 grids is finally selected in this work since moving from it to a finer one with twice as many grids led to less than 2% difference between the GCI values of the axial velocity.

Table 1
Summary of the GCI calculation for selected variables on different meshes.

Area-averaged mean variables	GCI_{21} (%)	GCI_{32} (%)	GCI_{43} (%)
Axial velocity	6.4	2.6	1.3
Tangential velocity	0.4	0.1	0.02
Temperature	0.1	0.06	0.01

4. Model validation

The experimental data pertinent to the Gatton tower, as reported in [6], are used to validate the numerical model. In the experiment, 27 temperature sensors were evenly mounted at three cross-sections, i.e., the top layer (14 m height above the heat exchanger), middle layer (7 m height above the heat exchanger), and bottom layer (0.8 m height above the heat exchanger), respectively. The air temperature distribution inside the tower was thus measured based on the average value during the test time. Here, to validate our results, we employ the average air temperature on the bottom layer, T_{bl}, for 5 different conditions. The heat exchanger temperature is calculated based on the mean water temperature in the experiments. The average air temperature on the bottom layer, T_{bl}, is shown in Table 2, in which E and N represent the experimental and numerical data, respectively. The subscript 1 and 2 stand for the k-ϵ realizable model and the RNG k-ϵ model, respectively. As seen, the numerical results calculated by k-ϵ realizable model generally show better agreements with the experimental ones, with the maximum error less than 3%.

5. Results and discussion

Fig. 5(a) indicates another successful comparison of our numerical prediction for the air temperature against the experimental data collected, in the presence of the cold air inflow, for the Gatton tower as reported in [6]. The average air temperatures on the top layer, the middle layer, the bottom layer, as well as the ambient temperature were measured. Note the cold air inflow incurs under windless conditions, as presented that wind speed blow 2 m/s in

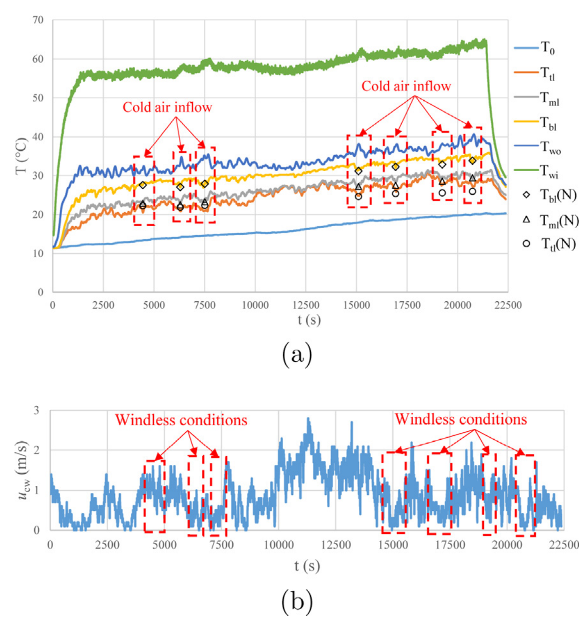

Fig. 5. Cold air inflow observed in experiments: (a) temperature change and several numerical data; (b) crosswind speed change.

Table 2
Comparison between experimental and numerical results.

Case	T_0 (°C)	T_{hx} (°C)	T_{bl} (E)(°C)	T_{bl} $(N_1 \mid N_2)$ (°C)	Error 1 | 2
1	18.20	41.70	33.00	33.45 | 32.68	1.4% | 1.0%
2	20.20	38.20	32.20	31.98 | 31.35	0.7% | 2.6%
3	21.40	44.70	36.70	36.07 | 35.71	1.7% | 2.7%
4	24.00	41.85	36.60	36.10 | 35.85	1.4% | 2.0%
5	27.00	44.65	38.80	37.90 | 36.97	2.3% | 4.7%

Fig. 5(b). One also notes that, the cold inflow effect would be insignificant with the increase of the crosswind [6]. Subsequent numerical studies on Gatton tower also indicate that the cold air inflow will be negligible when the crosswind speed exceeds 2 m/s [47,48]. However, as experimental data show, the cold air inflow incurs on windless conditions, leading to obvious rises on the water outlet temperature which consequently reduces the cooling performance of the tower. Thus, it is necessary to investigate and prevent this phenomenon.

5.1. Cold air inflow formation

Fig. 6 shows the time-dependent heat rejection rate. As observed, the tower experiences four stages after starting. The first one is the start-up process, during which the heat exchanger starts from natural convection to forced convection, as indicated in [37]. After then a short period of pseudo-steady state is found, which is supposed to be the steady state when there is no cold air inflow. The third stage is in the period of the cold air inflow penetration. At this stage, a 33% decrease in the heat rejection rate occurs within 150 s, which is significant. The final stage is the steady state with a significant cold inflow.

For a more comprehensive understanding of the problem, temperature contours overlayed with the velocity vectors at selected time steps are demonstrated. Fig. 7(a) is for an early time step ($t = 130$ s) while Fig. 7(b) marks the beginning of the cold air inflow ($t = 190$ s), and Fig. 7(c) relates to ($t = 340$ s) when the cold air inflow reaches its maximum depth. Fig. 7(a) clearly illustrates two vortices formed inside the tower adjacent to the wall. The lower vortex is behind the solid ring, while the upper one is right above the tower throat. The ambient air enters the tower due to buoyancy as it crosses the heat exchanger, right above the plane on top of the heat exchanger, the flow experiences an expansion loss caused by the increases in the flow area. The flow area is obstructed by the heat exchangers and the solid ring. The latter is impermeable hence there is a local pressure difference over that cross section causing a recirculation zone in that area. This is how the lower vortex is formed, while the upper one is generated by the accumulation of negative vorticity due to the sufficient axial adverse pressure gradient as a result of the divergent shape above the tower throat. Both vortices oppose the draft. Meanwhile, the draft is accelerated by the buoyancy effect after it exits the tower, leading to a continuously narrowing effect of the hot plume. This narrowing effect is especially obvious in short NDDCTs at which the updraft velocity is low. Here the radial temperature gradient is so large that some of the cold air even mixes with the hot air before the draft leaves the tower exit. At the second selected time step, Fig. 7(b), as the flow develops inside the tower, the upper vortex becomes stronger, and thereby the vorticity adjacent to the wall cannot diffuse fast enough into the main flow region. Instead, the cold air mixing with the hot plume near the tower tip is induced and merged with the growing vortex. This is when the cold air starts penetrating into the tower and influencing the temperature distribution inside the tower. Subsequently, the reversed flow reaches the lower vortex to merge and form a larger downward flow motion, and the cold inflow penetrates straight to the solid ring and heat exchanger of the tower. The third selected time step when the cold inflow completely intrudes into the tower is shown in Fig. 7(c). Here, the temperature distribution inside the tower is drastically changed, and the heat rejection rate through the heat exchanger is significantly reduced.

5.2. Cold inflow process in the presence of swirl

The axisymmetric swirl is created by adding tangential momentums in the source zone; see Fig. 2. The effect of input swirl intensity of the source zone on the unsteady NDDCT performance is analysed first with a fixed aspect ratio of the source zone ($Ar_\phi = 0.07$). The comparison among input swirl intensities ($\Phi_\theta = 1, 2, 3, 4$) is shown in Fig. 8. In general, the input swirl

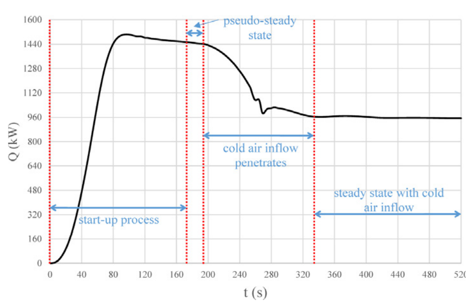

Fig. 6. The heat rejection rate as a function of time.

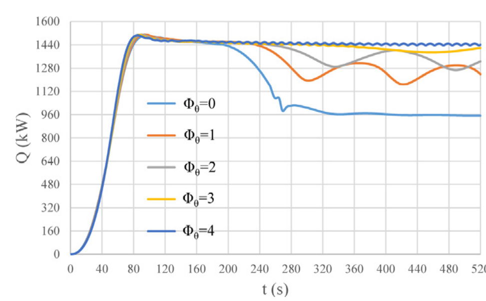

Fig. 8. The heat rejection rate as a function of time with different input swirl intensities.

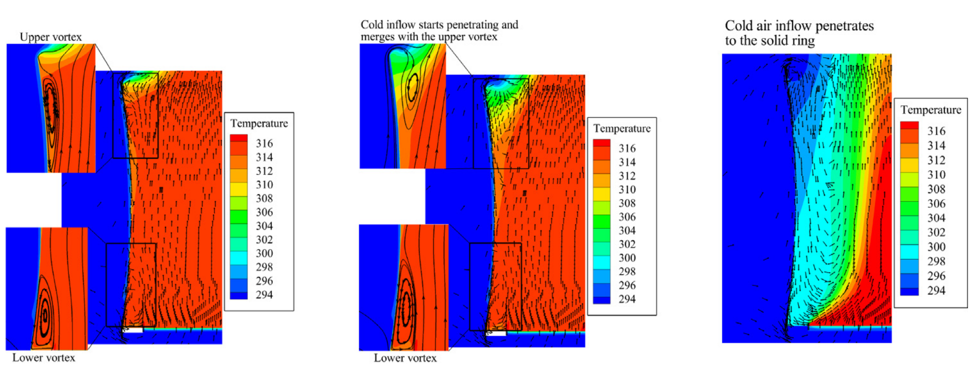

Fig. 7. Temperature contour and velocity vectors: (a) $t = 130$ s; (b) $t = 190$ s; (c) $t = 340$ s.

apparently improves the heat rejection rate of the tower by reducing the cold inflow effects in all cases. In addition, oscillations are also observed after swirl is introduced, and specifically, the more intensive the swirl, the lower the amplitude. Another interesting observation is that, the heat rejection rate reaches its peak earlier as swirl intensity increases, indicating that swirl also have favourable effects on the start-up process. This influence generally occurs after 50 s, before which an overlap is observed, implying the adopted swirl barely influences the free convection stage during the start-up process.

The temperature contours overlayed with the velocity vectors when the heat rejection rate reaches minimum values due to the cold air inflow penetration at selected cases are also demonstrated in Fig. 9. As presented, the maximum cold air inflow penetration depth reduces as swirl intensity increases. In addition, results, pertinent to Fig. 8, also show that the heat rejection rates start oscillating after the cold air inflow penetrates with cases ($\Phi_\theta = 1.0$, $\Phi_\theta = 2.0$). This is because, after the cold air intrudes, the hot air velocity through the tower decreases, resulting in an increase in the air temperature of the main flow due to the fixed heat exchanger temperature. This increased main flow temperature will also enhance the buoyancy effect, which pushes back against the cold air inflow. During this process, the hot air velocity, in turn, increases while the temperature decreases, and when it is not capable of pushing the cold air inflow, the cold air intrudes back again and thus the oscillation appears. However, in the absence of swirl, the cold air inflow penetrates straight to the solid ring, and then the hot air, although its temperature increases as presented in the temperature contour in Fig. 7(c), cannot push the cold air inflow back anymore.

As mentioned previously, the swirl can prevent the reversed flow from penetrating straight to the solid ring. To understand that, the temperature contours overlayed with the axial velocity vectors for the cases with different swirl intensities before cold inflow incurs are illustrated in Fig. 10. It is observed that the lower vortex is almost eliminated but another boundary layer separation followed by reattachment is adjacent to the tower wall above the solid ring in the case with $\Phi_\theta = 1.0$. This separation also disappears when Φ_θ reaches 2.0. As a result of the reduced or eliminated lower vortex, the larger downward motion caused by the mergence between the cold air inflow and the lower vortex is not formed anymore. Hence, the cold air inflow does not penetrate straight to the solid ring, and oscillation appears as demonstrated before. Additionally, the more intensive the swirl the smaller the upper vortex to a point that the upper vortex disappears when Φ_θ reaches 3.0, as shown in Fig. 10(c). The disappearance of the upper vortex is also correlated to a negligible cold air inflow as seen in Fig. 8.

As discussed above, swirl can reduce the adjacent-wall vortices caused by the specific structure of the tower, but this might not be the whole reason for swirl decreasing the cold air inflow effect, since the cold air inflow phenomenon was also found in buoyant duct in cylinder shape where the adjacent-wall vortices are absent [8]. However, it is doubtless that the vortices adjacent to the wall tend to intensify the cold air inflow effect since the downward flow motion becomes larger once the penetrated cold air merges with the vortices. In addition to the vortices reduced by swirling motions, the boundary layer thickness is also decreased by introducing swirl due to the radial pressure gradient changed by the centrifugal effect, as indicated in the theoretical study [27,28]. It was also mentioned that the cold air inflow effect is reduced by

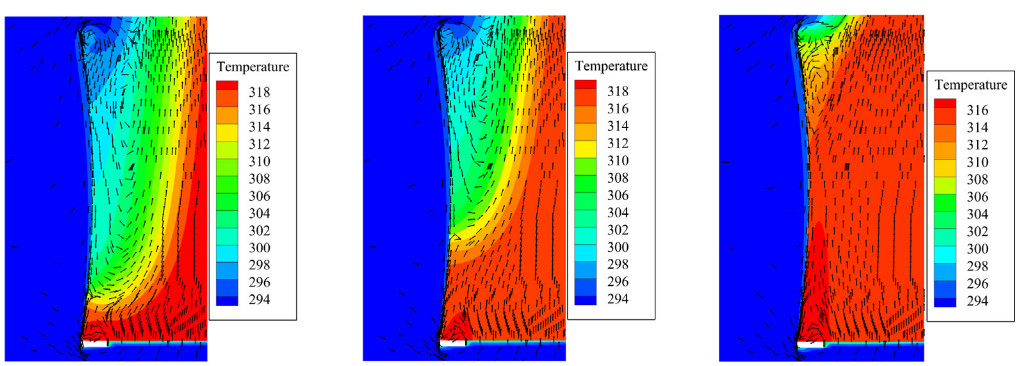

(a) (b) (c)

Fig. 9. Temperature contour and velocity vectors at the lowest heat rejection rate: (a) $\Phi_\theta = 1.0$; (b) $\Phi_\theta = 2.0$; (c) $\Phi_\theta = 3.0$.

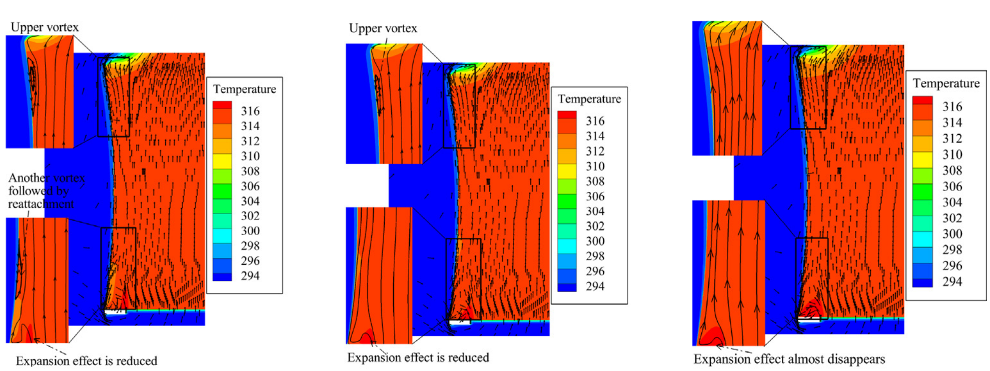

(a) (b) (c)

Fig. 10. Temperature contour and velocity vectors before the cold inflow penetrates ($t = 130$ s): (a) $\Phi_\theta = 1.0$; (b) $\Phi_\theta = 2.0$; (c) $\Phi_\theta = 3.0$.

thinning the boundary layer thickness [16]. This is reasonable since the cold air inflow is initially formed by the negative buoyancy caused by the density difference between the cold air in the periphery of the tower tip and the hot air inside the tower; see Fig. 7(b). Once the boundary layer thickness is reduced, the narrowing effect on the hot plume above the tower exit can also be alleviated, resulting in a decreased negative buoyancy and such that the cold air inflow effect is reduced. Hence, u^+ as a function of y^+, at different swirl input intensities associated with the law of wall is illustrated in Fig. 11. It should be noted that these profiles are selected at the middle layer where the vortices adjacent to the wall are absent, and the time step before the cold air inflow penetrates ($t = 130\,\text{s}$) such that the axial velocity profiles can be observed without perturbations. As seen, more intensive the swirl is, quicker the axial velocity profile flattens out away from the wall. Consequently, the local axial velocity near the wall tends to decrease, which also results in an increase in the local axial velocity away from the wall because of the continuity.

We now move on to consider the effects of the aspect ratio of the source zone. Considering practical limitation for the swirl generator inside the tower, the numerical value of the aspect ratio is restricted to 0.35 in this study. Thus, several aspect ratios of the source zone ($Ar_\phi = 0.07, 0.14, 0.21, 0.28, 0.35$) are compared in this section, while the dimensionless input swirl intensity value remains 1, respectively. As shown in Fig. 12, with the increase of the aspect ratio of the source zone, the cold inflow is also delayed and reduced, indicating that the cold air inflow is also influenced by the "volume" of the source zone. One might argue that, as the height of the source zone increases, the mixing losses are more severe hence the swirl intensity decreases resulting in a higher average swirl intensity adjacent to the tower wall, which causes the delay and reduction of the cold air inflow as mentioned before.

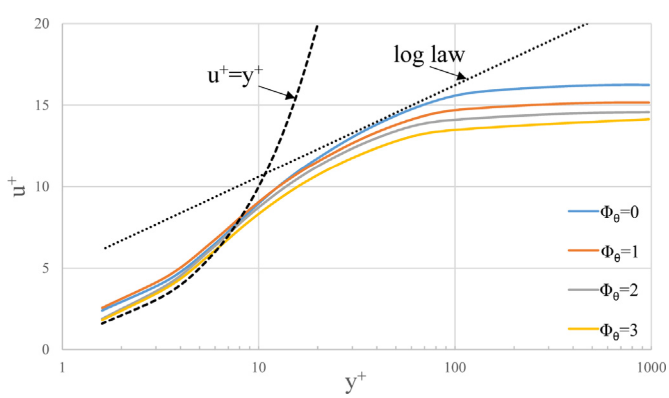

Fig. 11. The dimensionless axial velocity profile before the cold inflow penetrates ($t = 130\,\text{s}$) at different input swirl intensities.

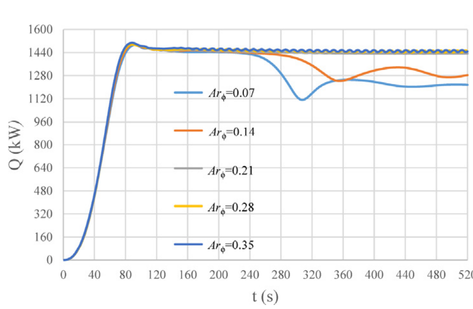

Fig. 12. The heat transfer rate as a function of time at different aspect ratios of the source zone ($\Phi_\theta = 1.0$).

5.3. Energy consumption estimation of the input swirl

We have investigated the use of swirl to avoid the cold air inflow. Hence, it is necessary to estimate the energy consumption of the swirl source for practical applications. The ideal energy consumption for the source can be calculated by:

$$Q_\phi = \int_V \phi_\theta u_\theta dV = 2\pi H_\phi \phi_\theta \int_{R_1}^{R_2} u_\theta dr \tag{21}$$

The input values of the tangential source terms ϕ_θ corresponding to the selected dimensionless swirl intensities ($\Phi_\theta = 1, 2, 3$) are $1.62\,\text{N/m}^3, 3.24\,\text{N/m}^3, 4.86\,\text{N/m}^3$, respectively. The corresponding tangential velocities cannot be known in advance, so they are collected after the tower reaches its steady state. Then the power consumption can be calculated from Eq. (21). Fig. 13 presents the heat rejection rate associated with the energy consumption rate for several cases. As presented, the heat rejection rate improved by swirl is four orders of magnitudes higher than the energy consumption to generate swirl. Even with a very low power conversion efficiency, the gain in the tower heat rejection rate is much higher than the required energy to generate the swirl.

For the industrial application, it is necessary to totally eliminate the cold air incursion rather than just delaying or reducing it. As discussed before, both the input swirl intensity and the aspect ratio

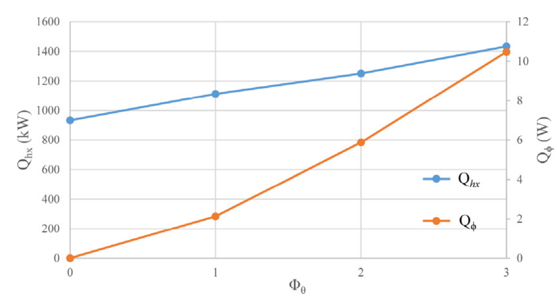

Fig. 13. The heat rejection rate associated with energy consumption as functions of the dimensionless input swirl intensity ($Ar_\phi = 0.07$).

Table 3
Critical input swirl intensities of source zones with different aspect ratios and their energy consumptions.

Ar_ϕ	Φ_θ	Q_ϕ (W)
0.07	3.1	12.0
0.14	2.3	11.7
0.21	1.1	9.8
0.28	0.9	10.7
0.35	0.8	11.3

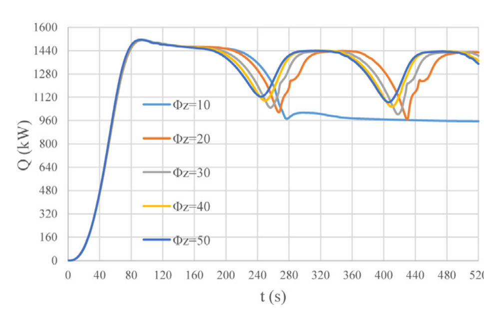

Fig. 14. The heat rejection rate as a function of the time at different input vertical source intensities ($Ar_\phi = 0.07$).

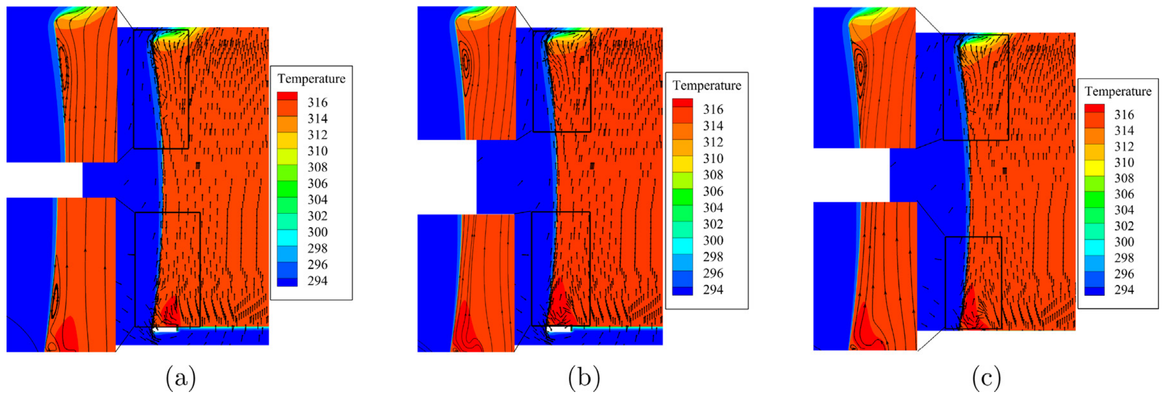

Fig. 15. Temperature contour and velocity vectors before the cold inflow penetrates ($t = 130$ s): (a) $\Phi_z = 10$; (b) $\Phi_z = 30$; (c) $\Phi_z = 50$.

influence the cold inflow process. For each case with a fixed aspect ratio, there exists a critical input swirl intensity at which the cold air inflow effect can be reduced to the minimum. These critical input swirl intensities and the associated energy consumptions are illustrated in Table 3. As seen, the energy consumptions are $\sim O(10\,W)$. The energy consumption can then be minimized though the difference is negligibly small.

5.4. Comparison with vertical source terms

It could be argued that perhaps the cold inflow can be controlled by adding vertical momentum instead of tangential momentum in the source zone. Hence, in the source zone, the vertical source term is added in the axial momentum (Eq. (6)), and the dimensionless vertical source intensity is defined in the similar way with Eq. (12) by replacing the tangential source term with the vertical one. Then the time-dependent heat rejection rate with different vertical source intensities is also investigated. It is however found that the axial momentum is much harder to be transferred from the external force, since the resistance is considerably higher in the axial direction than in the tangential direction. It is observed from Fig. 14, the vertical source can barely reduce the cold inflow despite the numerical values for the vertical intensities are one order of magnitude higher than those of tangential cases. In addition, a more intensive vertical source leads to an earlier cold inflow penetration but a lower amplitude in the heat rejection rate change.

The temperature contours overlayed with velocity vectors selected at 130 s with different vertical source intensities are shown in Fig. 15. As seen, the lower vortex caused by the expansion effect is highly reduced by the vertical source, while the upper one grows larger as vertical intensity increases. This is reasonable since the axial direction is not parallel to the direction along the wall, and specifically, with the divergent shape above the tower throat, increasing the axial velocity near the wall certainly results in an earlier boundary layer separation. Consequently, the earlier boundary layer separation and the correlated larger vortex induce the cold air inflow near the tower tip earlier with the increase in the vertical source intensity.

Hence, addition of swirl is investigated as an alternative approach which has proved beneficial. The energy consumption to generate swirl is also compared with the extra gain through the increased heat rejection rate. A comparison between tangential and vertical swirl was also made clearly indicating the superiority of the former. As for practical methods to create those source terms, we recommend installing a radial fan with many blades, which have the same size as the cross-section size of the source zone, for the tangential source, while arranging lots of axial fans uniformly above the solid ring for the vertical source.

6. Conclusions

In this study, a 2-D axisymmetric model for a short NDDCT is established and numerical investigation of the cold air inflow phenomenon is carried out. Major conclusions are listed below:

- It is found that the cold air inflow forms after a short period of pseudo-steady state after the start-up process and significantly decreases the heat rejection rate of the NDDCT.
- Vortices, adjacent to the wall, caused by the specific tower structure tend to intensify the cold air inflow effect, but they can be reduced by introducing swirling motions from a source zone mounted on the solid ring around the heat exchanger. Thus, the cold air inflow effect is alleviated.
- Swirl is able to reduce the boundary layer thickness, which was indicated to be capable of decreasing the cold air inflow effect [8]. This further explains why introducing swirl inside the tower, especially near the wall, has beneficial effect on reducing the cold air inflow influence.
- The energy consumption by the swirl source is much lower in comparison with the tower performance the swirl increases, indicating a reasonable industrial applicability.
- Finally, compared with the vertical source intensity, tangential source is more efficient in transferring momentum since there is less resistance along the tangential direction than in the vertical direction, proving that it is more applicable to reduce the cold air inflow by inputting swirl instead of vertical source in the short NDDCT.

Declaration of Competing Interest

The authors declare that there is no conflict of interest.

Acknowledgements

This research was performed as part of the ARC DECRA (Discovery Early Career Research Award) project DE190101253. The authors would like to thank Australian Solar Thermal Research Institute (ASTRI) and China Scholarship Council (CSC) for their financial support. The authors also acknowledge the financial support from Spanish Ministry of Economy Industry and Competitiveness, the State Research Agency (AEI) and the European Union by

European Regional Development Fund – Feder Project ENE2017-83729-C3-3-R.

References

[1] Australia's off-grid clean energy market research paper, AECOM, Canberra, 2014.
[2] Y. Lu, Small natural draft dry cooling towers for renewable power plants.
[3] M. Gao, F.-Z. Sun, K. Wang, Y.-T. Shi, Y.-B. Zhao, Experimental research of heat transfer performance on natural draft counter flow wet cooling tower under cross-wind conditions, Int. J. Therm. Sci. 47 (7) (2008) 935–941.
[4] Y. Lu, Z. Guan, H. Gurgenci, Z. Zou, Windbreak walls reverse the negative effect of crosswind in short natural draft dry cooling towers into a performance enhancement, Int. J. Heat Mass Transf. 63 (2013) 162–170.
[5] Y. Lu, Z. Guan, H. Gurgenci, K. Hooman, S. He, D. Bharathan, Experimental study of crosswind effects on the performance of small cylindrical natural draft dry cooling towers, Energy Convers. Manage. 91 (2015) 238–248.
[6] X. Li, Numerical and Experimental Study of Small Natural Draft Dry Cooling Tower for Concentrating Solar Thermal Power Plant (Ph.D. thesis), The University of Queensland, 2018.
[7] K. Tanimizu, K. Hooman, Natural draft dry cooling tower modelling, Heat Mass Transf. 49 (2) (2013) 155–161.
[8] O. Jörg, R. Scorer, An experimental study of cold inflow into chimneys, Atmos. Environ. 1 (6) (1967) 645–654.
[9] V. Modi, F. Moore, Laminar separation in buoyant channel flows, J. Fluid Mech. 177 (1987) 37–47.
[10] V. Modi, K. Torrance, Experimental and numerical studies of cold inflow at the exit of buoyant channel flows, J. Heat Transf. 109 (2) (1987) 392–399.
[11] E. Sparrow, G. Chrysler, L. Azevedo, Observed flow reversals and measured-predicted nusselt numbers for natural convection in a one-sided heated vertical channel, J. Heat Transf. 106 (2) (1984) 325–332.
[12] R. Khanal, C. Lei, Flow reversal effects on buoyancy induced air flow in a solar chimney, Sol. Energy 86 (9) (2012) 2783–2794.
[13] T. Fisher, K. Torrance, Experiments on chimney-enhanced free convection, J. Heat Transf. 121 (3) (1999) 603–609.
[14] C.C. Chu, M.M. Rahman, A method to achieve robust aerodynamics and enhancement of updraft in natural draft dry cooling towers, in: ASME 2009 Heat Transfer Summer Conference Collocated with the InterPACK09 and 3rd Energy Sustainability Conferences, American Society of Mechanical Engineers, 2009, pp. 817–823.
[15] D.G. Kröger, Air-cooled Heat Exchangers and Cooling Towers, vol. 1, PennWell Books, 2004.
[16] C.-M. Chu, M.M. Rahman, S. Kumaresan, Effect of cold inflow on chimney height of natural draft cooling towers, Nucl. Eng. Des. 249 (2012) 125–131.
[17] C.-M. Chu, M.M. Rahman, S. Kumaresan, Improved thermal energy discharge rate from a temperature-controlled heating source in a natural draft chimney, Appl. Therm. Eng. 98 (2016) 991–1002.
[18] R. Fox, A. McDonald, Effects of swirling inlet flow on pressure recovery in conical diffusers, AIAA J. 9 (10) (1971) 2014–2018.
[19] C. Hah, Calculation of various diffuser flows with inlet swirl and inlet distortion effects, AIAA J. 21 (8) (1983) 1127–1133.
[20] K.L. So, Vortex phenomena in a conical diffuser, AIAA J. 5 (6) (1967) 1072–1078.
[21] P. Clausen, S. Koh, D. Wood, Measurements of a swirling turbulent boundary layer developing in a conical diffuser, Exp. Therm. Fluid Sci. 6 (1) (1993) 39–48.
[22] Y. Senoo, N. Kawaguchi, T. Nagata, Swirl flow in conical diffusers, Bull. JSME 21 (151) (1978) 112–119.
[23] S. Armfield, C. Fletcher, Comparison of k–ϵ and algebraic reynolds stress models for swirling diffuser flow, Int. J. Numer. Meth. Fluids 9 (8) (1989) 987–1009.
[24] S.W. Armfield, N.-H. Cho, C.A. Fletcher, Prediction of turbulence quantities for swirling flow in conical diffusers, AIAA J. 28 (3) (1990) 453–460.
[25] E. Kurkin, V. Shakhov, Algebraic and k-ϵ turbulence model comparison in the problem of the boundary layer on the walls of a rotating axisymmetric diffuser, Procedia Comput. Sci. 65 (2015) 133–139.
[26] C. From, E. Sauret, S. Armfield, S. Saha, Y. Gu, Turbulent dense gas flow characteristics in swirling conical diffuser, Comput. Fluids 149 (2017) 100–118.
[27] A. Najafi, M. Saidi, M. Sadeghipour, M. Souhar, Boundary layer solution for the turbulent swirling decay flow through a fixed pipe: Sbr at the inlet, Int. J. Eng. Sci. 43 (1–2) (2005) 107–120.
[28] R. Maddahian, A. Kebriaee, B. Farhanieh, B. Firoozabadi, Analytical investigation of boundary layer growth and swirl intensity decay rate in a pipe, Arch. Appl. Mech. 81 (4) (2011) 489–501.
[29] A. Klimenko, Strong swirl approximation and intensive vortices in the atmosphere, J. Fluid Mech. 738 (2014) 268–298.
[30] M.H. Kashani, K. Dobrego, Heat and mass transfer in the over-shower zone of a cooling tower with flow rotation, J. Eng. Phys. Thermophys. 86 (6) (2013) 1490–1499.
[31] M.H. Kashani, K. Dobrego, Influence of flow rotation within a cooling tower on the aerodynamic interaction with crosswind flow, J. Eng. Phys. Thermophys. 87 (2) (2014) 385–393.
[32] Y. Lu, A. Klimenko, H. Russell, Y. Dai, J. Warner, K. Hooman, A conceptual study on air jet-induced swirling plume for performance improvement of natural draft cooling towers, Appl. Energy 217 (2018) 496–508.
[33] T.-H. Shih, W.W. Liou, A. Shabbir, Z. Yang, J. Zhu, A new k-e eddy viscosity model for high reynolds number turbulent flows, Comput. Fluids 24 (3) (1995) 227–238.
[34] FLUENT User's Guide, ANSYS. Inc., USA, 2009.
[35] F. Kreith, O. Sonju, The decay of a turbulent swirl in a pipe, J. Fluid Mech. 22 (2) (1965) 257–271.
[36] A.I. Bosioc, C. Tanasa, S. Muntean, R. Susan-Resiga, Pressure recovery improvement in a conical diffuser with swirling flow using water jet injection, in: Proceedings of the Romanian Academy, Series A: Mathematics, Physics, Technical Sciences, Information Science, ISSN 14549069.
[37] P. Dong, X. Li, Y. Sun, K. Hooman, Z. Guan, Y. Dai, H. Gurgenci, Numerical investigation of the influence of local effects on the transient start-up process of natural draft dry cooling towers in dispatchable power plants, Int. J. Heat Mass Transf. 133 (2019) 166–178.
[38] H. Reuter, D. Kröger, Computational fluid dynamics analysis of cooling tower inlets, J. Fluids Eng. 133 (8) (2011) 081104.
[39] R. Al-Waked, M. Behnia, The performance of natural draft dry cooling towers under crosswind: Cfd study, Int. J. Energy Res. 28 (2) (2004) 147–161.
[40] K. Hooman, Dry cooling towers as condensers for geothermal power plants, Int. Commun. Heat Mass Transf. 37 (9) (2010) 1215–1220.
[41] A. Escue, J. Cui, Comparison of turbulence models in simulating swirling pipe flows, Appl. Math. Model. 34 (10) (2010) 2840–2849.
[42] F. Kaya, I. Karagoz, Performance analysis of numerical schemes in highly swirling turbulent flows in cyclones, Curr. Sci. (00113891) 94 (10).
[43] H. Chen, V. Patel, Near-wall turbulence models for complex flows including separation, AIAA J. 26 (6) (1988) 641–648.
[44] W. Rodi, Experience with two-layer models combining the k-epsilon model with a one-equation model near the wall, in: 29th Aerospace sciences meeting, 1991, p. 216.
[45] G. Gerolymos, I. Vallet, Implicit computation of three-dimensional compressible navier-stokes equations using k-epsilon closure, AIAA J. 34 (7) (1996) 1321–1330.
[46] P.J. Roache, Quantification of uncertainty in computational fluid dynamics, Ann. Rev. Fluid Mech. 29 (1) (1997) 123–160.
[47] P. Dong, X. Li, K. Hooman, Y. Sun, J. Li, Z. Guan, H. Gurgenci, The crosswind effects on the start-up process of natural draft dry cooling towers in dispatchable power plants, Int. J. Heat Mass Transf. 135 (2019) 950–961.
[48] K. Hooman, Theoretical prediction with numerical and experimental verification to predict crosswind effects on the performance of cooling towers, Heat Transf. Eng. 36 (5) (2015) 480–487.